





---

21

22 **Abstract:**

23 Surface soil moisture (SSM) is crucial for understanding the hydrological process of  
24 our earth surface. Passive microwave (PM) technique has long been the primary tool  
25 for estimating global SSM from the view of satellite, while the coarse resolution  
26 (usually  $>10$  km) of PM observations hampers its applications at finer scales.  
27 Although quantitative studies have been proposed for downscaling satellite PM-based  
28 SSM, very few products have been available to public that meet the qualification of 1-  
29 km resolution and daily revisit cycles under all-weather conditions. In this study, we  
30 developed one such SSM product in China with all these characteristics. The product  
31 was generated through downscaling the AMSR-E/AMSR-2 based SSM at 36-km,  
32 covering all on-orbit time of the two radiometers during 2003-2019. MODIS optical  
33 reflectance data and daily thermal infrared land surface temperature (LST) that had  
34 been gap-filled for cloudy conditions were the primary data inputs of the downscaling  
35 model, so that the “all-weather” quality was achieved for the 1-km SSM. Daily images  
36 from this developed SSM product have quasi-complete coverage over the country  
37 during April-September. For other months, the national coverage percentage of the  
38 developed product is also greatly improved against the original daily PM observations,  
39 through a specifically developed sub-model for filling the gap between seams of  
40 neighboring PM swaths during the downscaling procedure. The product is well  
41 compared against *in situ* soil moisture measurements from 2000+ meteorological  
42 stations, indicated by station averages of the unbiased RMSD ranging from 0.052



---

43 vol/vol to 0.059 vol/vol. Moreover, the evaluation results also show that the developed  
44 product outperforms the SMAP-Sentinel (Active-Passive microwave) combined SSM  
45 product at 1-km, with a correlation coefficient of 0.55 achieved against that of 0.40 for  
46 the latter product. This indicates the new product has great potential to be used for  
47 hydrological community, agricultural industry, water resource and environment  
48 management.

## 49 **1. Introduction**

50 Surface soil moisture (SSM) is one of the most important variables that dominate  
51 the mass and energy cycles of earth surface system. Satellite-based SSM datasets of  
52 sufficiently fine spatio-temporal resolutions over large-scale areas have significant  
53 implication on improved investigations at various research fields including  
54 hydrological signature identification, agricultural yield production estimation,  
55 drought/waterlogging monitoring and warning, as well as weather prediction and future  
56 climate analysis. Microwave bands with centimeter-level or longer wavelengths (X-  
57 band, C-band, and L-band) are currently identified as the primary band channels  
58 suitable for SSM observations from view of satellite, due to their high penetration  
59 capabilities through cloud layers and vegetation canopies. In terms of sensor types,  
60 microwave SSM detection includes passive microwave (radiometer-based) techniques  
61 and active microwave (radar, scatterometer) techniques. Satellite-based passive  
62 microwave (PM) radiometers, e.g. the Soil Moisture Active Passive (SMAP), the Soil  
63 Moisture and Ocean Salinity (SMOS), and the Advance Microwave Scanning



---

64 Radiometer-2 (AMSR-2), can obtain SSM observations at a revisit interval of 1-3 days,  
65 with relatively poor native spatial resolutions of tens of kilometers. Active microwave  
66 (AM) such as radar can achieve kilometer-level and even finer resolution of  
67 observations targeting at the earth surface. However, this usually sacrifices the swath  
68 width of radar configuration, because of which, most satellite-based synthetic aperture  
69 radars (SAR) have an obviously longer global revisit cycle (usually longer than 5 days,  
70 e.g. Sentinel-1 SAR data) than the typical radiometers. Moreover, AM radar backscatter  
71 signals are extremely sensitive to speckle noise (Entekhabi et al., 2016), as well as  
72 influence from soil roughness, vegetation canopy structure and water content (Piles et  
73 al., 2009). All above influential factors have seriously impeded the use of AM radar  
74 techniques or combination of passive/active microwave datasets for producing high  
75 spatial resolution SSM products with a frequent revisit.

76       Apart from microwave signals, solar reflectance or ground emission signals  
77 originated from optical and infrared band domains also have the potential to reflect  
78 SSM variation. Based on optical/infrared bands, however, SSM is typically estimated  
79 based on indirect relationships through intermediate variables like soil evaporation,  
80 vegetation condition, or soil thermal inertia. To overcome the spatio-temporally  
81 instable performance on SSM modelling that might be brought by such indirect  
82 relationships, they are typically fused with the PM SSM datasets. In this manner, it can  
83 well reconcile the advantage of PM observations with respect to its high sensitivity to  
84 SSM variation, as well as that of optical/infrared observations with respect to its finer  
85 spatial resolutions at kilometer- or even hectometer-levels. Such data fusion techniques



---

86 are also known as downscaling techniques of PM remote sensing SSM. Archetypal  
87 downscaling models include the “triangle feature space (UTF)”-based models  
88 (Chauhan et al., 2003; Choi and Hur, 2012; Sanchez-Ruiz et al., 2014), the  
89 “DISaggregation based on a Physical And Theoretical scale CHange (DISPACTH)”  
90 model (Merlin et al., 2010; Merlin et al., 2005; Merlin et al., 2013; Merlin et al., 2008),  
91 and the UCLA model (Peng et al., 2016). The physics of these models are mainly based  
92 on the response of SSM variation to changes in soil evaporation or land surface  
93 evapotranspiration. Another significant branch of such downscaling models are based  
94 on the sensitivity of SSM to soil thermal inertia, which is quantified by diurnal LST  
95 difference estimated from thermal-infrared wave bands (Fang and Lakshmi, 2013; Fang  
96 et al., 2018).

97 Sabaghy et al. (2020) have shown that using optical and infrared data can achieve  
98 finer-resolution SSM estimates which are better consistent with ground soil moisture  
99 records, compared with using the radar datasets. Moreover, considering the short revisit  
100 cycle (daily) of optical/infrared sensors onboard typical polar-orbit satellites, using  
101 optical/infrared datasets to downscale PM SSM should be among the optimal methods  
102 for obtaining SSM data with high spatio-temporal resolutions over national, continental,  
103 or global scales. On the other hand, satellite remote sensing SSM products that are  
104 characterized by 1-km resolution of daily revisit intervals and stable long time series  
105 dating back to at least 15-20 years ago, are urgently required for accelerating the  
106 development of various research fields, especially agriculture industry, water resources  
107 management, and hydrological disaster monitoring (Sabaghy et al., 2020; Mendoza et



---

108 al., 2016). However, very seldom sets of such data products are publicly available to  
109 the remote sensing research community because of the following drawbacks,. First,  
110 there is a serious lack of cloud-free optical/infrared imagery, which means the method  
111 cannot deliver any SSM downscaling under cloudy/rainy weather. Second, most of the  
112 above-mentioned optical/infrared-data-based downscaling methods were mainly  
113 evaluated at regional or even smaller scales. This might raise concern on the  
114 universality of those methods. For example, the DISPATCH method has been  
115 recognized to be less effective in humid (energy-limited) regions compared with in arid  
116 and semi-arid (water-limited) regions (Molero et al., 2016; Song et al., 2021; Zheng et  
117 al., 2021), whilst another experiment (Kim and Hogue, 2012) shows that the UTF-based  
118 methods are found even inferior to the DISPATCH in a typical water-limited region in  
119 North America.

120 To improve the above-mentioned issues, we produced all-weather daily SSM data  
121 products at 1-km resolution all over China during 2003-2019, based on fusion of  
122 multiple remote sensing techniques, including reconstruction of optical/infrared  
123 observations under cloud as well as an improved PM SSM downscaling methodology  
124 proposed in our previous study (Song et al., 2021). The major objectives of this study  
125 include

126 (i) to better serve and investigate the land surface hydrology processes and their  
127 sophisticated interactions to human society at multi-scale (from national to regional)  
128 resolutions in China because the country covers about 1/15 of the global terrestrial area  
129 with about 1/5 of the world population, and



---

130 (ii) to provide a methodology framework that can inspire future studies on  
131 generating similar SSM datasets all over the globe, based on the plentifulness of  
132 resources on climate type, land covers, and topography in China.

133

## 134 **2. Methods and Materials**

### 135 **2.1 Datasets**

#### 136 2.1.1 PM SSM data

137 Spatial downscaling of PM SSM is the fundamental theory for constructing the  
138 target finer-resolution data product in this study. Therefore, the native retrieval  
139 accuracy of the coarse-resolution PM SSM data product, based on which the  
140 downscaling procedures are performed, is considerably crucial to the performance of  
141 the downscaled data product (Busch et al., 2012; Im et al., 2016; Kim and Hogue, 2012).

142 Although the L-band PM brightness temperature (TB) observed by satellite missions  
143 such as SMAP or SMOS are considered more suitable for SSM retrieval compared with  
144 C- or X-band TB, both above missions started their space operations after 2010s. This  
145 means that to obtain downscaled SSM of longer historical periods, we still require to  
146 rely on other C-/X-band-based radiometers which started their operations earlier than  
147 SMAP and SMOS. An optimal satellite PM TB observation system dating back to  
148 earlier years of this century is composed of the “Advanced Microwave Scanning  
149 Radiometer of the Earth Observing System (AMSR-E)”, together with its successor of  
150 AMSR-2. AMSR-E operated during 2002-2011 onboard the Aqua satellite which is



---

151 governed by National Aeronautics and Space Administration (NASA), whilst AMSR-  
152 2 is operating onboard the Global Change Observation Mission1-Water (GCOM-W1)  
153 satellite developed by the Japan Aerospace Exploration Agency (JAXA) since 2012.

154 Several classical PM SSM retrieval algorithms have been applied to the afore-  
155 mentioned “AMSR series (including AMSR-E and AMSR-2)” TB for generating long-  
156 term global SSM products at 25 km (Table 1), including the JAXA algorithm (Fujii et  
157 al., 2009; Koike et al., 2004), the “Land Parameter Retrieval Model (LPRM)” algorithm  
158 (Song et al., 2019b; Meesters et al., 2005; Owe et al., 2001), and the algorithm  
159 developed by the University of Montana (UMT) (Jones et al., 2009; Du et al., 2016). A  
160 recent AMSR-based night-time SSM product during 2002-2019 has been produced  
161 through a neural network trained against SMAP descending SSM (hereafter referred to  
162 as “NN-SM product”) (Yao et al., 2021). The global validation results show that this  
163 NN-SM product is better than the JAXA and LPRM products.

164 Besides, the NN-SM has also been compared with another long-term ~25-km all-  
165 weather SSM dataset generated through the European Space Agency (ESA)’s Climate  
166 Change Initiative (CCI) program. The ESA-CCI SSM product is different from the rest  
167 products mentioned above in that it was implemented by fusion of observations from  
168 comprehensive AM- and PM-based satellite sensors, rather than only relying on the  
169 radiometers of AMSR series. According to Yao et al. (2021), the ESA-CCI SSM has  
170 slightly better validation accuracy than the NN-SM product, but the number of available  
171 observations per pixel cell in an entire year is much smaller for the ESA-CCI SSM in  
172 Southeast China. In view of all above coarse-resolution SSM data products, we finally





173 selected the NN-SM product to implement the following spatial downscaling  
 174 procedures rather than the ESA-CCI SSM, to make a balance between data accuracy  
 175 and data availability per year. We have also made additional evaluations within China  
 176 in Section Appendix-A to ensure the relatively outstanding performance of the NN-SM  
 177 product as described above.

178 Table 1 Information of all-weather microwave remote sensing coarse-resolution SSM data  
 179 products that can be potentially downscaled to obtain high resolution SSM.

| Name                    | Resolution                                | Satellite radiometers<br>involved                                 | Data availability (url)   |
|-------------------------|---|---|---|
| NN-SM<br>product        | 36 km (by the<br>EASE Grid<br>projection) | AMSR-E/ AMSR-2<br>(2002-2011, 2012-present)                       | <a href="https://data.tpdc.ac.cn/en/data/c26201fc-526c-465d-bae7-5f02fa49d738/">https://data.tpdc.ac.cn/en/data/c26201fc-526c-465d-bae7-5f02fa49d738/</a> |
| ESA-CCI v6.1<br>product | 0.25°                                     | AMSR-E/ AMSR-2/<br>SMOS/ WindSat/ SMMR/<br>SSM/I/ TMI (1978-2020) | <a href="https://www.esa-soilmoisture-cci.org/v06.1_release">https://www.esa-soilmoisture-cci.org/v06.1_release</a>                                       |
| JAXA product            | 0.25° / 0.1°                              | AMSR-E/ AMSR-2<br>(2002-2011, 2012-present)                       | <a href="https://gportal.jaxa.jp/">https://gportal.jaxa.jp/</a>   |
| LPRM<br>product         | 0.25° / 0.1°                              | AMSR-E/ AMSR-2<br>(2002-2011, 2012-present)                       | <a href="https://search.earthdata.nasa.gov/">https://search.earthdata.nasa.gov/</a>   |
| UMT product             | 25 km (by the<br>EASE Grid<br>projection) | AMSR-E/ AMSR-2<br>(2002-present)                                  | <a href="http://files.ntsg.umt.edu/data/LPDR_v2/">http://files.ntsg.umt.edu/data/LPDR_v2/</a>   |

180



---

181 2.1.2 Optical remote sensing data and digital elevation model (DEM)

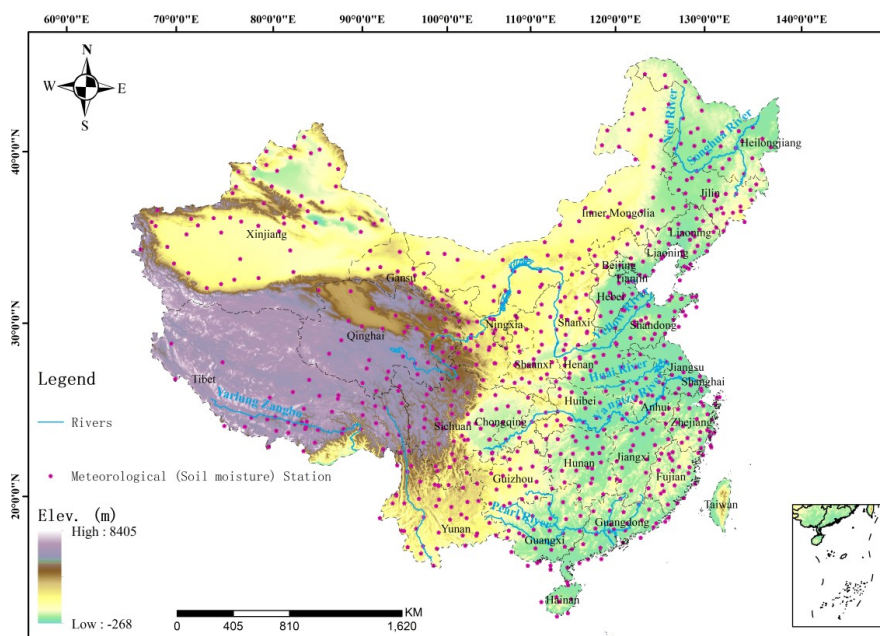
182       Optical remote sensing datasets provide finer spatial texture information on the  
183 daily basis for the downscaling purpose of PM SSM. Such data that can be used as  
184 inputs of our SSM product processing line are mainly provided by the Moderate-  
185 resolution Imaging Spectroradiometer (MODIS) onboard the Terra and Aqua satellites.  
186 Specifically, they involve the 1-km daily night-time Aqua MODIS LST product  
187 (MYD21A1N.v061) and the 500-m daily “Bidirectional Reflectance Distribution  
188 Function (BRDF)” - Adjusted Reflectance dataset (MCD43A4.v061). MYD21A1 LST  
189 data can be recognized as a crucial proxy of land surface thermal capacity (Fang et al.,  
190 2013) and soil evaporative rate (Merlin et al., 2008). The MCD43A4 nadir reflectance  
191 product, with view angle effect corrected using the BRDF model, is capable to provide  
192 observations from visible to shortwave-infrared bands that can characterize water  
193 content variation of the bare soils as well as the vegetation canopy. Overall, the above-  
194 mentioned datasets were selected primarily because they deliver indicators (land  
195 surface thermal capacity, soil evaporative rate, or vegetation condition) that can well  
196 response to soil moisture dynamics from different aspects. Prior to be employed for  
197 SSM downscaling, conventional pre-processing procedure of pixel quality check was  
198 applied for both optical products by screening out pixels not classed as “good quality”,  
199 according to the 8-bit “Quality Assessment (QA)” field of each spectral band. Moreover,  
200 to normalize their natively different spatial resolutions, all MCD43A4 based reflectance  
201 values at the 500-m pixel level were upscaled to the sinusoidally projected MODIS 1-  
202 km grids using their spatial averages.



203 Apart from MODIS optical remote sensing data, all 90-m DEM tiles generated by  
204 the NASA Shuttle Radar Topography Mission (SRTM; <http://srtm.csi.cgiar.org/>, last  
205 access: July 10, 2020) were mosaicked over the entire China and then employed as  
206 another essential input variable for the procedures as described by Section 2.2.2 below.  
207 Similar to that applied to the MCD43A4 product, spatial upscaling in correspondence  
208 to the MODIS 1-km grids is also an indispensable pre-processing step for the mosaicked  
209 DEM data.

### 210 2.1.3 Ground validation data

211



212  
213 Fig. 1 The provincial-level administration map of China superposed with topographic information, as  
214 well as general locations for the 756 basic meteorological stations (<http://data.cma.cn/>, last access:



---

215 January 20, 2021) that provide partial benchmark measurements for SSM and LST validation in this  
216 study.

217 We utilized ground soil moisture measurements for validating the downscaled  
218 remote sensing SSM product. The ground measurements are derived from 2417  
219 meteorological stations (including 756 basic stations of the National Climate  
220 Observatory and 1661 regionally intensified stations) of over China, as partially shown  
221 in Fig. 1. The soil moisture measurement devices in these stations, with uniform  
222 observation standards, are instrumented under the national project of “Operation  
223 Monitoring System of Automatic Soil Moisture Observation Network in China (Wu et  
224 al., 2014 )”, the construction of which has been led by China Meteorological  
225 Administration since 2005. Until 2016, all stations have been in operation for  
226 automatically observing hourly in situ soil moisture dynamics at eight different depth  
227 ranges (0-10 cm, 10-20 cm, 20-30 cm, 30-40 cm, 40-50 cm, 50-60 cm, 70-80 cm, 90-  
228 100 cm). In our current study, ground measurements matching the shallowest depth  
229 range (0-10 cm) from the initial time of each station until the end of 2019 are employed  
230 as validation benchmark of the satellite SSM retrievals. At the temporal dimension,  
231 measurements made at 1:00 A.M. and 2:00 A.M are averaged, in order to match the  
232 mean satellite transit time of 1:30 A.M. for AMSR descending observations.

233 Moreover, 0-cm top ground temperatures are simultaneously measured at all these  
234 meteorological stations on the daily basis, at the local time windows of 2:00 A.M./P.M.  
235 and 10:00 A.M./P.M., respectively. We therefore exploited such measurements  
236 recorded at 2:00 A.M. to validate the cloud gap-filled night-time (~1:30 A.M.) LST



---

237 estimates over the Aqua-MODIS based 1-km pixels containing these stations (see  
238 Section 2.2.2). Our primary validation period covers the entire years of 2017, 2018, and  
239 2019.

#### 240 2.1.4 Ancillary SSM products for comparison

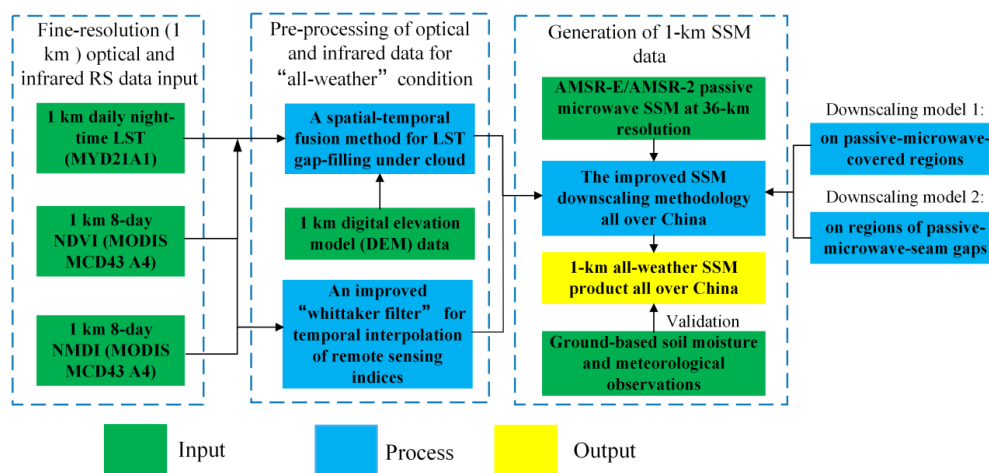
241 In order to comprehensively demonstrate the validation performance of our  
242 proposed SSM product, there is necessity to make an inter-comparison against similar  
243 existing datasets. In this regard, we introduced the Level2 SMAP/Sentinel Active-  
244 Passive combined SSM product on 1-km earth-fixed grids, i.e., the SPL2SMAP\_S\_V3  
245 dataset (Das et al., 2020), and used its validation performance against in-situ  
246 measurements throughout the years of 2017, 2018, and 2019, as a baseline to better  
247 evaluate our proposed SSM product. The SPL2SMAP\_S\_V3 dataset contains global  
248 SSM at resolutions of 3 km and 1 km respectively, which were disaggregated from the  
249 SMAP SSM retrievals of 36-km/9-km footprints in conjunction with the high-  
250 resolution Sentinel-1 C-band radar backscatter coefficients (Das et al., 2019). To our  
251 knowledge, this dataset is possibly the only publicly available product which can  
252 provide global remote sensing SSM estimates at the 1-km resolution. The sentinel  
253 backscatter coefficient inputs for this product are only those received in the descending  
254 orbit scenes (at ~6:00 A.M. of local time), whilst the closest SMAP SSM retrievals  
255 from either ascending (at ~6:00 P.M. of local time) or descending orbits are used to  
256 spatially match up with the sentinel-1 scene. It is noticed that at the descending  
257 observation time the soil moisture vertical profile has approached a hydrostatic balance



258 (Montaldo et al., 2001), thereby providing the optimal chance for soil moisture fusion  
259 and validation with observations at different soil depths. Therefore, we only selected  
260 the 1-km disaggregated SSM estimates based on descending SMAP SSM retrievals (i.e.,  
261 the subset with field name of ‘disagg\_soil\_moisture\_1 km’ in the SPL2SMAP\_S\_V3  
262 dataset). Meanwhile, the 10-cm-depth in-situ soil moisture measurements observed at  
263 6:00 A.M. were employed as the validation benchmark, in a manner similar to that  
264 applied to our proposed SSM product (Section 2.1.3).

## 265 2.2 Methodology

266 The general methodological framework for producing the all-weather daily 1-km  
267 SSM product is shown as in Fig. 2, with details described in the following context of  
268 this section.



269  
270

Fig. 2 The overall methodological framework of this study.

271 2.2.1 Reconstruction of thermal-infrared LST and remote sensing (vegetation)  
272 indices under cloud

273 Reconstruction of missing pixels under cloud in the optical remote sensing input  
274 datasets is the prerequisite for achieving the “all-weather” property of the final



---

275 downscaled SSM output. For reconstructing thermal-infrared LST, we adopted the  
276 cloud gap-filling method as proposed by our previous study (Song et al., 2019a). This  
277 method, also referred to as a typical “spatio-temporal data fusion” (STDF) method  
278 (Dowling et al., 2021), was built using clear-sky LST observations of spatially  
279 neighboring pixels observed at proximal dates, with concurrent NDVI and DEM also  
280 employed as additional data inputs. The STDF method can be expressed as follows:

$$281 \quad LST_{t_1}^* = a \times LST_{t_0}^* + b \times NDVI_{t_1}^* + c \times DEM^* + d \quad (1)$$

282 Where the superscript “\*” indicates that this variable has been normalized to the range  
283 0 to 1.0 (Song et al., 2019a), based on the maximum and minimum values of that  
284 variable found across China (excluding invalid values representing states of snow, ice,  
285 and water bodies). Parameters  $a$ ,  $b$ ,  $c$ , and  $d$  are coefficients fitted between all pixels  
286 with clear-sky LST estimates on a specific date  $t_1$  ( $LST_{t_1}^*$ ) and their counterparts on  
287 one proximal date,  $t_0$  ( $LST_{t_0}^*$ ).  $NDVI_{t_1}^*$  indicates the corresponding (normalized) NDVI  
288 on the  $t_1$  date calculated using the MCD43A4 daily product. After deriving the  
289 coefficients of  $a$ ,  $b$ ,  $c$ , and  $d$ , Equation (1) was used to fill all cloudy MODIS LST pixels  
290 on the  $t_1$  date. For any  $t_1$  date included in the study period, the  $t_0$  date was iterated among  
291 all neighboring dates of  $t_1$  meeting the condition  $|t_0 - t_1| \leq 30$  (from the nearest date to  
292 the furthest date). The average of estimated LST values for  $t_0$  was then taken where a  
293 cloud gap pixel was filled more than once (based on the iterative  $t_0$  dates). The iteration  
294 was stopped when the fraction of pixels with effective LST values on  $t_1$  was equal to or  
295 exceeded 0.99.

296 An important flaw of this STDF method should be noticed with regard to  
297 potentially existential bias of the cloud gap-filled LST outputs, because the outputs  
298 represent theoretically reconstructed LST under clear sky rather than under the real  
299 cloudy condition. Another of our previous studies (Dowling et al., 2021) concerning



---

300 this STDF method proposed a follow-up step, which incorporated PM-derived surface  
301 temperature, to adjust that bias. In our current production pipeline, however, this  
302 follow-up step for cloud bias adjustment in LST was not carried out. This is mainly  
303 because the gap-filled LST outputs are intended for SSM downscaling. The  
304 downscaling techniques as proposed in Section 2.2.1 was developed based on the  
305 “universal triangle feature (UTF)” theory (Carlson et al., 1994). In the UTF, clear-sky  
306 LST was employed to quantify the land surface evaporation when vegetation cover  
307 density was fixed. The degree of land surface wetness was then predicted implicitly  
308 through soil evaporation degree and surface soil thermal inertia. Under cloudy  
309 conditions, however, the satellite observed LST would be a proxy of not only surface  
310 soil property, but also of that related to cloud liquid water and crystals in the  
311 atmospheric layers. In comparison, therefore, LST generated by the STDF alone for  
312 clear-sky conditions would be a more competent input variable for quantifying surface  
313 soil wetness under cloudy conditions. We have made additional evaluations to confirm  
314 the validity of this assumption, with the results elaborated in Section Appendix-B of  
315 this paper.

316 Reconstruction of the remote sensing vegetation indices under cloudy conditions,  
317 including NDVI and MNDI, was simply based on the modified time series filter of the  
318 Whittaker Smoother (MWS) as developed by Kong et al. (2019). This is reasonable  
319 because the dynamic trends of vegetation growth are relatively less volatile compared  
320 to LST on the daily basis, and can thus be gap-filled for missing values using a time-  
321 series-filtering-like algorithm.

322 2.2.2 Improved downscaling technique of SSM based on fusion of PM and  
323 optical/infrared data





324 The core component of the SSM downscaling methodology is an improved linking  
325 model between PM SSM and (fine-resolution) optical remote sensing observations.  
326 Since the model origins from our previous study (Song et al., 2021), herein we simply  
327 give its mathematical expression as follows:

$$328 \quad SSM = \frac{a \times \ln(1 - SEE)}{1 - b \times NMDI} + c \quad (2)$$

329 In Equation (2),  $SEE$  is a mathematical function of LST and the typical Normalized  
330 Difference Vegetation Index (NDVI), with its specific form described in Merlin et al.  
331 (2008). NMDI is another remote sensing index calculated as  
332  $\frac{R_{infr,860nm} - (R_{sw,1600nm} - R_{sw,2100nm})}{R_{infr,860nm} + (R_{sw,1600nm} - R_{sw,2100nm})}$  (Wang and Qu, 2007).  $R_{infr,860nm}$ ,  $R_{infr,1600nm}$ ,  
333 and  $R_{infr,2100nm}$  represent land surface reflectance signals derived from three different  
334 MODIS-MCD43A4 based near-infrared/shortwave-infrared bands, with their  
335 wavelengths centering at 860 nm, 1600 nm, and 2100 nm respectively. The parameters  
336  $a$ ,  $b$ , and  $c$  are empirical coefficients that represent background information of local  
337 soil texture and vegetation types. In Song et al. (2021), these coefficients have been  
338 fitted and calibrated based on multi-temporal observations at the PM pixel scale. In our  
339 current study, however, we have discovered that coupling of multiphase observations  
340 at both the spatial and the temporal dimensions can lead to more optimal solution of the  
341 coefficients, as they can produce downscaled SSM images with notably declined effect  
342 of ‘mosaic’ against the original PM 36-km pixels. Therefore, the modified optimal cost  
343 function  $\chi^2$  for deriving these coefficients is re-defined as follows:

$$344 \quad \chi^2 = \sum_{d=-5}^5 \sum_{i=0}^{N=7 \times 7} w_i \times (SSM_{ob,i,d} - SSM_{mod,i,d})^2 \quad (3)$$



---

345 Through the cost function, the spatial extent of each 36-km pixel  $P_0$  on any arbitrary  
346 date  $D_0$  obtains a unique set of coefficients. As shown by Equation (3), all pixels within  
347 the  $N=7 \times 7$  spatial window centered at  $P_0$  ranging from  $-5th$  day to  $5th$  day relative to  
348 the date of  $D_0$  were exploited.  $SSM_{ob}$  and  $SSM_{mod}$  denote the AMSR NN-SM 36-km  
349 SSM observations as well as SSM observations modelled by Equation (2) based on  
350 upscaled optical datasets, respectively.  $w_i$  is a weight coefficient used to ensure that  
351 neighboring observations near the centering pixel  $P_0$  play more dominating roles as  
352 compared with the far-end pixels in the cost function, considering the “Tobler’s First  
353 Law of Geography (Sui, 2004)” .  $w_i$  is calculated using an adaptive bi-square function:

$$354 \quad \begin{aligned} w_i &= \left[1 - \left(\frac{dis_i}{b}\right)^2\right]^2, dis_i < b \\ w_i &= 0, dis_i \geq b \end{aligned} \quad (4)$$

355 where  $dis_i$  indicates the distance between the  $i$ -th pixel and the centering pixel  $P_0$ .  $b$  is  
356 named as the adaptive kernel bandwidth of the bi-square function (Duan and Li, 2016),  
357 and is optimized as 200 km through using a cross validation method as recommended  
358 by Brunson et al. (1996).

359 With the linking model obtained, we can subsequently utilize the spatial  
360 downscaling relationship function to produce 1-km high resolution SSM. The  
361 downscaling relationship function is constructed by transforming the linking model into  
362 its Taylor expansion formula and preserving all components with respect to the input  
363 optical variables of the linking model at first and second orders. This relationship is  
364 inspired from Malbêteau et al. (2016) and Merlin et al. (2010), and is mathematically  
365 described below:



$$\begin{aligned}
 366 \quad SSM_{1\text{-km}} &= SSM_{36\text{km}} + \left(\frac{\partial SSM}{\partial SEE}\right)_{36\text{km}} \times (SSE_{1\text{km}} - \langle SSE \rangle_{36\text{km}}) + 0.5 \times \left(\frac{\partial^2 SSM}{\partial SEE^2}\right) \times (SSE_{1\text{km}} - \\
 367 \quad &\langle SSE \rangle_{36\text{km}})^2 + \left(\frac{\partial SSM}{\partial NMDI}\right)_{36\text{km}} \times (NMDI_{1\text{km}} - \langle NMDI \rangle_{36\text{km}}) + 0.5 \times \left(\frac{\partial^2 SSM}{\partial NMDI^2}\right) \times \\
 368 \quad &(NMDI_{1\text{km}} - \langle NMDI \rangle_{36\text{km}})^2 \quad (5)
 \end{aligned}$$

369 In the above relationship,  $\langle \rangle$  denotes the operator of spatial averaging disaggregation  
 370 for the 1-km optical remote sensing input variables at the corresponding 36-km pixel,  
 371  $\frac{\partial SSM}{\partial SEE} \left(\frac{\partial^2 SSM}{\partial SEE^2}\right)$  and  $\frac{\partial SSM}{\partial NMDI} \left(\frac{\partial^2 SSM}{\partial NMDI^2}\right)$  respectively denoting the first-(second-) order  
 372 partial derivative of the linking model described in Equation (2).

373 It should be noticed that there exist middle-/low-latitude gap regions between  
 374 seams of neighboring daily AMSR-E(-2) swaths, indicating that  $SSM_{36\text{km}}$  in Equation  
 375 (5) is not always available on the daily basis (Song and Zhang, 2021a). For such PM-  
 376 seam gaps on a particular date  $t_0$ , the corresponding  $SSM_{36\text{km},t_0}$  in Equation (5) is  
 377 substituted by  $0.5 \times (SSM_{36\text{km},t_0+1} + SSM_{36\text{km},t_0-1}) + \Delta SSM_{36\text{km},t_0}$ . Herein  $SSM_{36\text{km},t_0-1}$   
 378 and  $SSM_{36\text{km},t_0+1}$  respectively denote the SSM estimate before and after the date of  $t_0$ .  
 379  $\Delta SSM_{36\text{km},t_0}$  is a component for correcting inter-day bias, with the following expression:

$$\begin{aligned}
 380 \quad \Delta SSM_{36\text{km},t_0} &= SSM(SEE_{36\text{km},t_0}, NMDI_{36\text{km},t_0}) - \\
 &0.5 \times (SSM(SEE_{36\text{km},t_0-1}, NMDI_{36\text{km},t_0-1}) + SSM(SEE_{36\text{km},t_0+1}, NMDI_{36\text{km},t_0+1})) \quad (6)
 \end{aligned}$$

381 In the above equation,  $SSM(SEE_{36\text{km}}, NMDI_{36\text{km}})$  denotes SSM that is directly  
 382 modelled based on Equation (1) using 36-km SEE and NMDI. The 36-km SEE and  
 383 NMDI are obtained via averaging the variables spatially from their native resolution at  
 384 1-km. If all  $SSM_{36\text{-km}}$  during the three consecutive days ( $t_0-1$ ,  $t_0$ , and  $t_0+1$ ) are missing  
 385 due to other extreme conditions like snow, ice, or surface dominated by substantially  
 386 large water bodies, the downscaling process cannot be fulfilled and all 1-km sub-pixels  
 387 with the  $SSM_{36\text{-km}}$  have to be set as null values.



---

388 2.2.3 Evaluation metrics

389 We employed the classic metrics of ‘Root Mean Square Difference (RMSD)’ and  
390 correlation coefficient (*r*-value) for evaluating satellite-based (SSM and LST) estimates  
391 against ground measurements. Herein RMSD is not referred to as ‘Root Mean Square  
392 Error (RMSE)’, although the latter term shares the same definition and has been used  
393 more commonly in previous studies. This is because the ground benchmark data may  
394 also present measurement uncertainties in practice. For SSM evaluation, the unbiased  
395 RMSD, or ubRMSD (Entekhabi et al., 2010; Molero et al., 2016), is calculated instead  
396 of RMSD in order to better investigate the time series similarity between satellite and  
397 ground soil moisture datasets by eliminating the systematic bias caused by spatial scale  
398 mismatch between them.

399 The above-mentioned classic metrics are primarily suitable to evaluate the  
400 absolute reliability of an independent remote sensing product. However, we also require  
401 another metric for characterizing the relative improvement of the downscaled SSM  
402 estimates against the original PM observations on capturing local soil moisture  
403 dynamics. For this purpose, we employed the “gain metric” of  $G_{down}$ , which was  
404 developed particularly by Merlin et al. (2015) for assessment of soil moisture  
405 downscaling methodology.  $G_{down}$  is a comprehensive indicator for evaluating gains of  
406 the downscaled SSM against the original coarse-resolution PM data in terms of their  
407 mean bias, bias in variance (slope), and time series correlation with ground benchmark.  
408 It has a valid domain between -1 and 1, with positive (negative) value indicating  
409 improved (deteriorated) spatial representativeness of the downscaled SSM against the



---

410 original PM data. Detailed definition and introduction of  $G_{down}$  are given in Equation  
411 (8) and Section 3.3 of Merlin et al. (2015).

## 412 **3. Results**

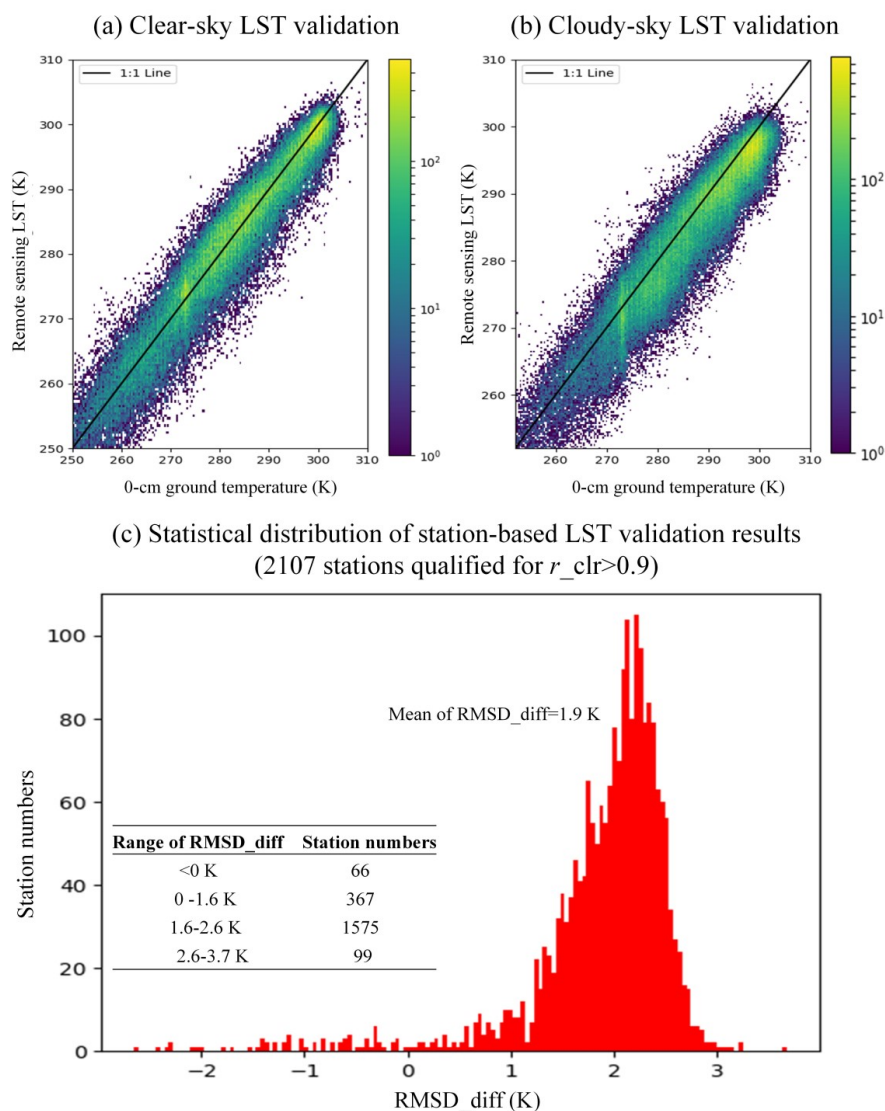
### 413 **3.1 Evaluation on reconstructed thermal-infrared LST under** 414 **cloud**

415 The meteorological-station-based validation of reconstructed 1-km thermal-  
416 infrared LST under cloud were preliminarily fulfilled, to ensure the high quality of input  
417 dataset variables for SSM downscaling. Since negative effects might be brought to this  
418 validation campaign by the potentially existing heterogeneity of the validated 1-km  
419 thermal-infrared remote sensing pixels, we firstly analyzed correlations between  
420 estimated and benchmark datasets at each station, only based on satellite remote sensing  
421 observations obtained under clear sky. Stations that have their correlation coefficients  
422 ( $r_{clr}$ ) lower than 0.9 herein have to be screened out because there exist higher chances  
423 of cross-scale spatial mismatch within and around these stations in terms of the land  
424 surface thermal properties. Among all 2417 stations (see Section 2.1.3) where 0-cm in-  
425 situ top-ground temperature measurements were available, we finally preserved 2107  
426 stations characterized by  $r_{clr} > 0.9$ . In the subsequent step, remote sensing LST under  
427 cloud and under clear-sky conditions were respectively validated at these stations, with  
428 the results revealed in Fig. 3. It is manifested through Fig. 3-(a) and -(b) that very close  
429 performances have been achieved between the clear-sky and the cloudy scenarios,  
430 especially considering their almost equally high validating correlations between 0.94-



---

431 0.95. For each independent station, we calculated the “RMSD difference (RMSD\_diff)”  
432 between the two scenarios, based on the formula of “ $RMSD_{clr} - RMSD_{cld}$  (the subscripts  
433 of ‘*clr*’ and ‘*cld*’ denote clear-sky and cloudy conditions separately)”. The statistical  
434 distribution of this RMSD difference with regard to different stations is shown in Fig.  
435 3-(c). Apparently, 1942 stations all over the country have obtained an RMSD difference  
436 value below 2.6 K, and the mean RMSD difference is only about 1.9 K. All above  
437 results have indicated small uncertainty of our night-time LST reconstruction algorithm  
438 proposed for cloudy conditions. The corresponsive uncertainty that could be propagated  
439 to downscaled SSM in this stage is analyzed below in Section 3.2.



440  
 441 Fig. 3 validation results of the cloud gap-filled LST in China. (a) Density plot of thermal infrared  
 442 LST under clear-sky condition compared to the 0-cm ground temperature measurements for all  
 443 stations. (b) Same to (a) but for thermal infrared LST under cloudy conditions. (c) Statistical  
 444 distribution of difference between RMSD of clear-sky LST and RMSD of gap-filled LST under cloudy  
 445 condition with regard to different meteorological stations over the study region.



---

446

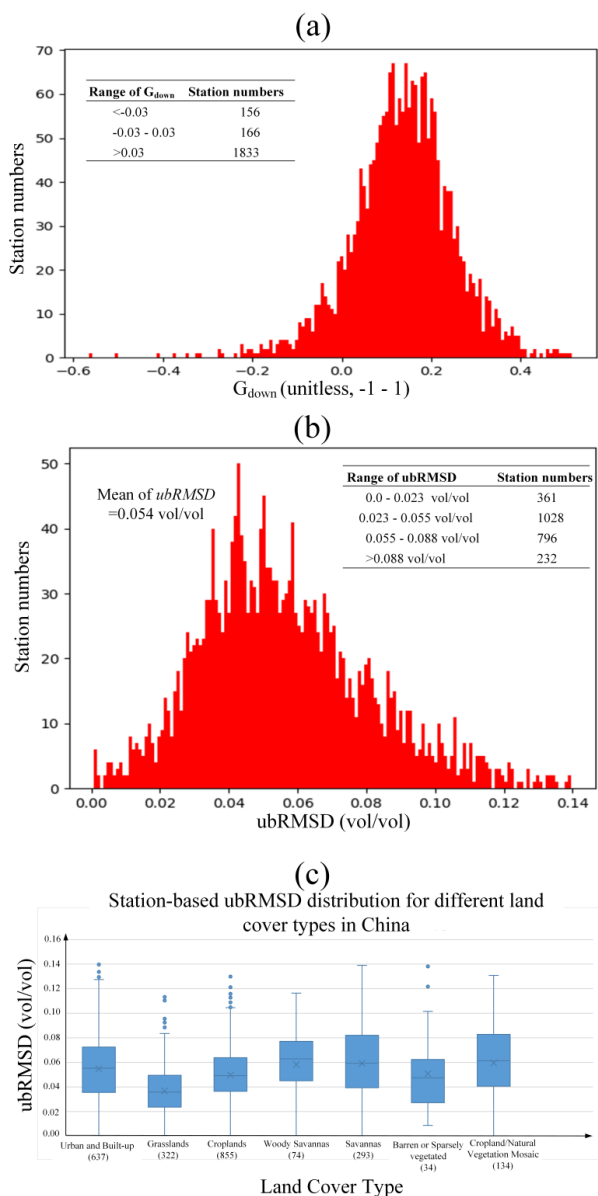
### 447 **3.2 Evaluation on the final 1-km SSM product**

448       The overall validation results of the finally downscaled 1-km SSM product is  
449 demonstrated in Fig. 4. Fig. 4-(a) shows that about 85% (N: 1833) of the total 2154  
450 stations (the remaining 263 stations are located in pixels with no effective PM  
451 observations and are thus removed) have obtained significantly positive downscaling  
452 gains ( $G_{down} > 0.03$ ). This hints that the 1-km SSM product can better capture the  
453 dynamic behaviors of local ground soil moisture data than the original 36-km PM NN-  
454 SM data, revealing higher spatial representativeness of the downscaled SSM data  
455 product over the country. According to Fig. 4-(b), the mean ubRMSD of all stations is  
456 about 0.054 vol/vol, while 90% of those stations have the number lower than 0.088  
457 vol/vol. In addition, we made another analysis concerning the possible influence of land  
458 cover types on SSM downscaling performance in Fig. 4-(c). The spatial information of  
459 land cover types was derived from the MODIS MCD12Q1  
460 ([10.5067/MODIS/MCD12Q1.006](https://doi.org/10.5067/MODIS/MCD12Q1.006)) IGBP-based land use image in 2019. For stations  
461 that experienced land use change throughout the years of the study period, the ubRMSD  
462 is only reported for data in the year of 2019. Clearly, better accuracies are observed  
463 mainly in grassland, cropland and bare soil surface, whilst relatively poorer  
464 performances (with averages of ubRMSD higher than 0.06 vol/vol) are seen in urban  
465 regions, (woody) savanna, and crop-to-natural-vegetation mosaic areas. Such a relative  
466 performance across land covers is logical because all the land cover types with their  
467 average ubRMSD higher than 0.06 vol/vol are characterized by lower hydrologic





468 homogeneity in terms of their definition, e.g. savanna, which is a mixture of grass and  
 469 tall trees, and urban areas, which are composed of impervious underlying surface.



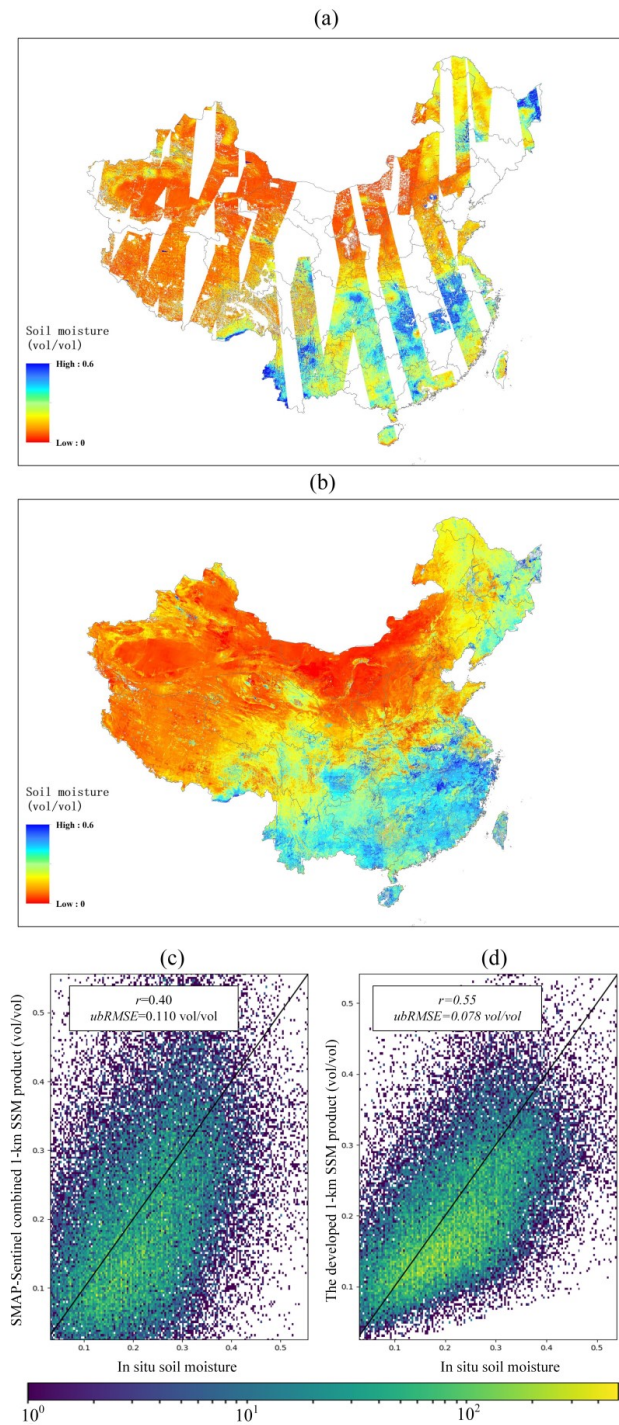
470  
 471 Fig. 4 General validation results of the currently developed SSM product. (a)  $G_{down}$  distribution for  
 472 different stations over China. (b) ubRMSD distribution for different stations over China. (c) ubRMSD



---

473 statistics reported for different land covers. The numbers in the parentheses of the x-axis labels  
474 represent the amount of meteorological stations corresponding to that specific land cover type.

475 In Fig. 5-(b) we employed the downscaled SSM image on April 9, 2018, as an  
476 example to demonstrate the spatial features of the developed product. Meanwhile, we  
477 also show the map of SMAP/Sentinel combined SSM (SPL2SMAP\_S\_V3) obtained  
478 from April 6 to April 11, 2018 in Fig. 5-(a), as a contemporaneous comparison reference.  
479 Clearly, the SPL2SMAP\_S\_V3 map has a much lower coverage percentage over the  
480 study region compared with the map of the currently developed product on one single  
481 date, even though the former was generated based on multi-date images. Both maps  
482 show similar spatial texture depicting the relatively dry climate in northwestern China  
483 compared with the humid climate in the Middle-lower Yangtze River Plain.  
484 Nevertheless, there also exist cases where the details in texture differ prominently, like  
485 that in the far northeastern end of the country. For the sake of further analysis on this  
486 point, results of the quantitative comparison as proposed in Section 2.1.4, is  
487 demonstrated in Fig. 5-(c) and Fig. 5-(d). The currently developed SSM product  
488 obtained a 0.078 vol/vol ubRMSD and a correlation coefficient of 0.55 against the in-  
489 situ soil moisture measurements, converging more apparently to the 1:1 line when  
490 compared with validation result of the SPL2SMAP\_S\_V3 dataset. As with the area of  
491 China, therefore, the currently developed product is superior to the global  
492 SMAP/Sentinel combined SSM in terms of both coverage percentage and estimate  
493 accuracy.





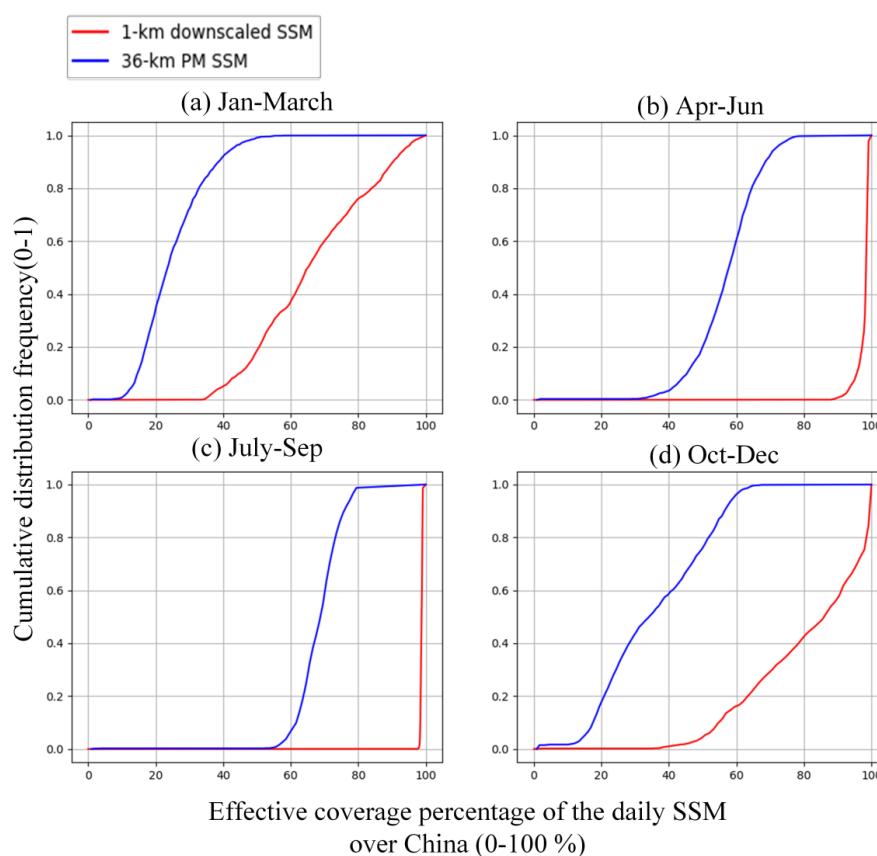
---

495 Fig. 5 Comparison results between the currently developed 1-km SSM product and the SMAP/Sentinel  
496 combined 1-km SSM (SPL2SMAP\_S\_V3). (a) SPL2SMAP\_S\_V3 SSM images over China at about  
497 6:00 a.m. synthesized by 6 continuous dates from April 6, 2018 to April 11, 2018. (b) The SSM image at  
498 1:30 a.m. of April 9, 2018 from the currently developed product. (c) Validation results of the  
499 SPL2SMAP\_S\_V3 product against in-situ soil moisture measurements over China for years of 2017,  
500 2018, and 2019. The black solid line is the 1:1 line. (d) Same to (c) but for validation of the currently  
501 developed SSM product.

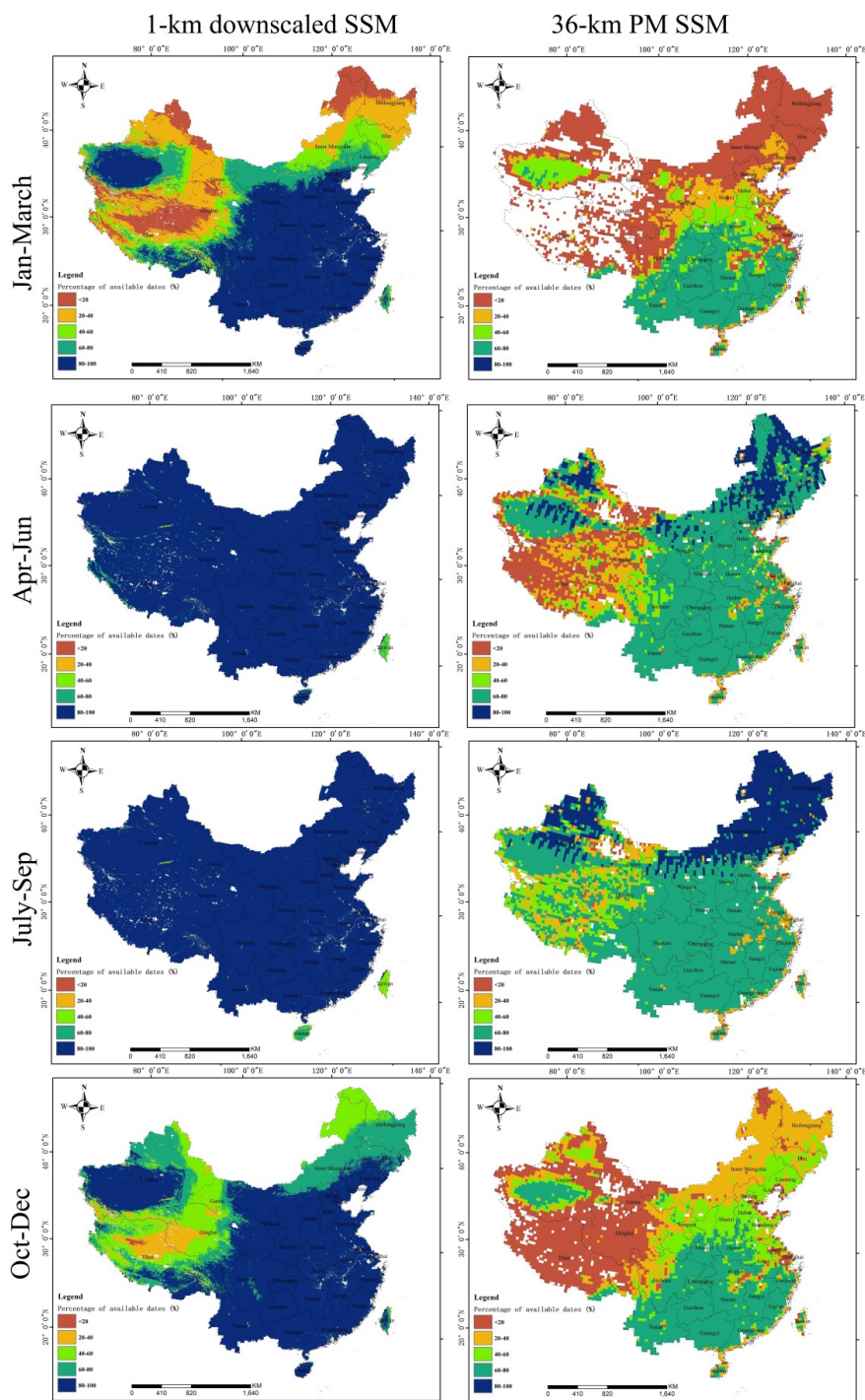
502 In Fig. 6, we display the cumulative distribution frequency of coverage  
503 percentages of the downscaled SSM product and of the original PM NN-SM product  
504 for each season. We should be noted that in this statistical scheme, pixels identified as  
505 static water body by the MODIS MCD12Q1 land cover type product were not  
506 considered in the denominator of the coverage percentage. Besides, the gap time  
507 between the respective on-orbit period of AMSR-E and of AMSR-2 (from October  
508 2011 to June 2012, during which there are no effective observations from the PM NN-  
509 SM product) were also excluded. It is apparent that in Fig. 6-(b) and -(c), almost all  
510 downscaled daily SSM images over the 16-17 years have achieved a coverage  
511 percentage close to 100% (at least above 95%). In comparison, the majority of the PM  
512 NN-SM daily images have their coverage percentages below 80% over the study region,  
513 primarily due to the PM-seam gaps particularly existing in low latitudes (see Section  
514 2.2.2). In Fig. 6-(a) and -(d), the percentages of effective pixels in both the PM and the  
515 downscaled SSM images are far lower than their counterparts in the other two  
516 subfigures. This is mainly ascribed to extreme meteorological conditions including



517 snow, ice, and frozen soils that are typically persistent throughout most of these  
518 specified months in the northwestern regions of China. Such conditions can impede  
519 reliable estimates of SSM based on all satellite remote sensing techniques in the current  
520 time.



521  
522 Fig. 6 Cumulative distribution frequency of our proposed SSM product against the original 36-km SSM  
523 product for different seasons. The period between October 2011 and June 2012 is excluded in the  
524 current statistics.  
525





---

527 Fig. 7 Spatial distributions on percentage of day numbers with available estimates for the currently  
528 developed 1-km SSM product and the original 36-km PM data during 2003-2019. The four different  
529 periods (i.e., January-March, April-June, July-September, October-December) of a year are treated  
530 respectively. The period between October 2011 and June 2012 is excluded.

531 The techniques behind coverage improvement of the downscaled SSM (against  
532 PM and optical data inputs) can be categorized into two classes, i.e. cloud gap-filling  
533 of the input optical datasets (see Section 2.2.1), as well as the filling of downscaled  
534 SSM in PM-seam gaps (see Section 2.2.2). Table 2 reports the specific validation results  
535 (using averages of all stations) of downscaled SSM in these coverage-improved  
536 conditions, relative to that generated without using any coverage improvement  
537 technique, in order to evaluate the propagated effect of such techniques on the final  
538 product. The very limited difference for ubRMSD values (0.053 vol/vol versus 0.056  
539 vol/vol) between cloudy and clear-sky conditions suggest that the cloud gap-filling  
540 techniques are generally compatible with SSM downscaling. To a certain extent, our  
541 pre-assumption that the theoretically hypothesized ‘clear-sky’ LST reconstruction is  
542 proved suitable for quantifying soil wetness variation. The downscaled SSM estimated  
543 for regions of PM-seam gaps have a slightly worse (but still acceptable) accuracy,  
544 considering its ubRMSD of 0.059 vol/vol compared to the 0.052 vol/vol ubRMSD of  
545 the PM-observed 1-km pixels. In summary of Fig. 6 and Table 2, the currently  
546 developed product has achieved a substantially improved spatial coverage against the  
547 original remote sensing input datasets, whilst successfully preserved the SSM  
548 downscaling accuracy of the observation-covered pixels at the same time.



549 Table 2 Comparisons between validation results for pixels under coverage-improved regions and  
550 for pixels under remote-sensing-observation-covered regions.

| Evaluation metric*      | Comparison between cloudy<br>and clear-sky conditions |                  | Comparison between passive<br>microwave (PM) observed regions<br>and regions of PM-seam gaps |              |
|-------------------------|---|------------------|--|--------------|
|                         | Clear-sky<br>condition                                | Cloudy condition | PM-observed<br>regions   | PM-seam gaps |
| ubRMSD (vol/vol)        | 0.053   | 0.056            | 0.052  | 0.059        |
| Correlation coefficient | 0.49  | 0.47             | 0.49   | 0.44         |

551 \*All evaluation metrics in this column indicate the average of all available stations

## 552 4. Discussion

### 553 4.1 Uncertainty on SSM evaluation between satellite- and 554 ground- scales

555 In this study, we made evaluations on remote sensing SSM products at different  
556 spatial resolutions, using measurements from 2000+ stations provided by the national-  
557 level soil moisture observation network of China as standard benchmark. Through the  
558 evaluations, a ubRMSD of 0.074 vol/vol is reported for the original 36-km NN-SM  
559 SSM product (Fig.A1-b). We notice that this result is considerably poorer if compared  
560 with another previous evaluation campaign targeting at the same product (Yao et al.,  
561 2021), which achieved a global RMSE (RMSD) of 0.029 vol/vol. However, this  
562 difference is not unexpected because the two campaigns were carried out in different  
563 regions of the world. Also, that particular study (Yao et al., 2021) was conducted based  
564 on completely different ground soil moisture observations provided by the International





---

565 Soil Moisture Network (ISMN) (Dorigo et al., 2021). Compared to the observation  
566 network employed in this study, the observation sites of ISMN are more intensively  
567 distributed as an “integrated soil moisture station” so as to provide spatially average  
568 soil moisture within a grid of tens of kilometers. In this regard, we admit that the ISMN  
569 is generally more professional in evaluating satellite PM-based SSM retrievals at a  
570 coarser resolution. But on the other hand, only a few ( $\leq 4$ ) of such “integrated stations”  
571 have been set up sporadically within China, making the ISMN data much less  
572 representative of our study region compared with the national-level soil moisture  
573 network of China exploited by our current study.

574       Although the higher RMSD of the national-level soil moisture network of China  
575 may indicate larger measurement uncertainty than the ISMN, the negative influence  
576 that might be imposed on our study purpose should be inconsequential. This is because  
577 we focus more on the relative validation performance of different SSM products, rather  
578 than on the absolute value of any evaluation metric including ubRMSD and correlation  
579 coefficient calculated against ground measurements. Specifically, the 1-km downscaled  
580 SSM obtained an average ubRMSD of about 0.054 vol/vol among different stations  
581 according to Fig. 4-(b). Besides, result of the evaluation in Fig. 5-(d) based on  
582 combination of multi-station ground measurements shows a global ubRMSD of 0.078  
583 vol/vol for this product. Overall, the above-mentioned results can be identified as at  
584 least comparable to the global (multi-station based) ubRMSD of 0.074 vol/vol of the  
585 original NN-SM data as they are evaluated against the same benchmark. Therefore,  
586 conclusion is safely drawn that the currently developed product preserves the retrieval



---

587 accuracy of the coarse-resolution NN-SM data, whilst improving the spatial  
588 representativeness of the latter product substantially according to the mostly positive  
589  $G_{down}$  values in Fig. 4-(a).

590 Moreover, one may also argue that the  $r$ -value of 0.55 for the currently developed  
591 product in Fig. 5-(d) is not sufficiently high compared with several previous studies  
592 (Wei et al., 2019; Sabaghy et al., 2020) obtaining  $r$ -values above 0.7 for temporal  
593 analysis of satellite remote sensing soil moisture. However, we should be noticed that  
594 these previous studies have conducted analyses respectively at the temporal and the  
595 spatial dimensions. Based on their results, the spatial analysis typically derived lower  
596  $r$ -values ( $<0.4$ ) compared to that at the temporal dimension. This is probably because  
597 the heterogeneity degree of remote sensing pixels can vary significantly across different  
598 sites. Since the evaluation in Fig. 5-(d) was deployed at the ‘spatio-temporal’ integrated  
599 dimensions, such an  $r$ -value is expected. This is also close to the global  $r$ -value of 0.6  
600 for validation of the coarse-resolution NN-SM product as reported in Yao et al. (2021).

#### 601 **4.2 Major novelty, unique profit, and future prospect of the** 602 **developed product**

603 Compared with the widely known active/passive microwave combined SSM  
604 product (e.g. the SPL2SMAP\_S\_V3) and other PM/optical-data combined counterparts  
605 which were also published recently but at the monthly scale (Meng et al., 2021), the  
606 major novelty of the currently developed product mainly lies in the fact that it has  
607 achieved progress on all of the three crucial dimensions of satellite remote sensing,



---

608 including the temporal revisit cycle (daily), the spatial resolution (1-km), and the quasi-  
609 complete coverage under all-weather conditions. To our knowledge, this has rarely been  
610 achieved by previously developed satellite soil moisture product at regional scales. For  
611 realization of the above-mentioned progresses, we have fused the SSM downscaling  
612 framework with other techniques including cloud gap-filling of thermal infrared LST,  
613 MWS-based temporal filtering of vegetation indices, as well as reconstruction of seams  
614 between neighboring PM swaths in low latitudes. The final SSM estimates under cloudy  
615 conditions and intersected with the PM-seam gaps were specially validated against the  
616 rest estimates under clear sky and in the regions covered by PM observations,  
617 respectively (Table 2). The comparable performances among all treatment groups  
618 herein confirm that the accuracy of the product is stable and consistent among all  
619 weather conditions.

620 With improvement achieved at the three dimensions, unique profit of the currently  
621 developed product can be taken by subsequent studies and various industrial  
622 applications. For example, the capability of this product can be investigated on  
623 capturing the short-term anomaly of local hydrological signals as well as improved  
624 monitoring on drought disasters, which used to be investigated mainly at a coarser  
625 resolution by PM SSM (Scaini et al., 2015; Champagne et al., 2011; Albergel et al.,  
626 2012). For another, taking advantage of its all-weather daily time series, the product  
627 can be utilized together with precipitation data to isolate and quantify the anthropic  
628 influence on regional water resources from the natural hydrological dynamics.  
629 Examples of such anthropic signals include agricultural irrigation activities, as well as



---

630 finer-scale information on agricultural crops which was previously interpreted based on  
631 PM-driven techniques (Song et al., 2018). In addition, we should realize the important  
632 role of soil moisture as a constraint for accurate estimation of surface  
633 evapotranspiration and runoff (Zhang et al., 2020; Zhang et al., 2019). Therefore, the  
634 profit of this product can be further enhanced if coupled with land-atmosphere coupled  
635 models to produce new insights into water-cycle processes of earth surface at a finer  
636 spatio-temporal scale.

637 In the future, the methodological framework proposed in this paper is prospective  
638 to be universally applied in other regions of the world to serve for better monitoring of  
639 the global surface wetness in the following studies. If applied in continental and global  
640 scales, however, the current process for gap-filling of PM seams may require further  
641 attention and improvement. In this study, SSM in regions intersected with PM-seam  
642 gaps were estimated using TB observations from PM swaths at neighboring dates (see  
643 Equation-5). Although the errors in the PM-seam gaps over China as reported by Table  
644 2 are only slightly larger compared to the PM-covered regions, they cannot be ignorable  
645 completely and may leave extra concern on the universality of this technique, especially  
646 in the low latitudinal tropical regions where the effect of PM-seam gap is more apparent  
647 than in our study area. Besides, another imperfection of this data product lies in the gap  
648 period between AMSR-E and AMSR-2. Considering the different systematic error  
649 patterns of various PM SSM products, we did not generate downscaled SSM based on  
650 other PM products (e.g. the SMOS SSM product) during this period but just left the  
651 period as null values. We suggest a more rigorous and universal inter-calibration



---

652 framework on different PM SSM products to be developed in the future for a long-term  
653 consistent 1-km downscaled SSM dataset.

## 654 **5. Conclusions**

655 This paper describes the main technical procedures of a recently developed remote  
656 sensing surface soil moisture (SSM) product over China covering the recent ten years  
657 and more. Based on combination of passive microwave SSM downscaling theory and  
658 other related remote sensing techniques, the product achieves multi-dimensional  
659 distinctive features including 1-km resolution, daily revisit cycle, and quasi-complete  
660 all-weather coverage. These were rarely satisfied completely by other existing remote  
661 sensing SSM product at regional scales. Validations were conducted against  
662 measurements from 2000+ automatic soil moisture observation stations over China.  
663 Overall, an average ubRMSE of 0.054 vol/vol across different stations is reported for  
664 the currently developed product. The mostly positive  $G_{down}$  values show this product  
665 has significantly improved spatial representativeness against the 36-km PM SSM data  
666 (a major source for downscaling). Meanwhile, it generally preserves the retrieval  
667 accuracy of the 36-km data product. Moreover, additional validation results show that  
668 the currently developed product surpasses the widely used SMAP-sentinel combined  
669 global 1-km SSM product, with a correlation coefficient of 0.55 achieved against that  
670 of 0.40 for the latter product. The methodological framework for product generation is  
671 promising to be applied at the continental and global scales in the future, and the product



---

672 is potential to benefit various research/industrial fields related to hydrological processes

673 and water resource management.

674



---

## 675 Appendix

### 676 A. Evaluation on different PM SSM products

677 We have made evaluations on the various AMSR-based SSM products (as shown  
678 in Table 1) covering the recent 10 years or longer, based on our soil moisture  
679 observation network all over China. The L-band based SMAP SSM dataset was also  
680 evaluated as a reference. The evaluation period covers the three years of 2017, 2018,  
681 and 2019. All AMSR-based 25-km grids were re-set to the SMAP 36-km grid system  
682 using the nearest resampling method. Only grids that contain equal or more than 4 soil  
683 moisture measurement stations were employed, in which, the grid-based PM SSM  
684 estimate was compared with average of measurements from all interior stations. Finally,  
685 53 grids were selected, as shown by the green color in Fig.A1-(g). For AMSR-based  
686 products, only the mid-night descending datasets were evaluated, whilst for the SMAP  
687 product, our evaluation only focused on its descending mode in the early morning.

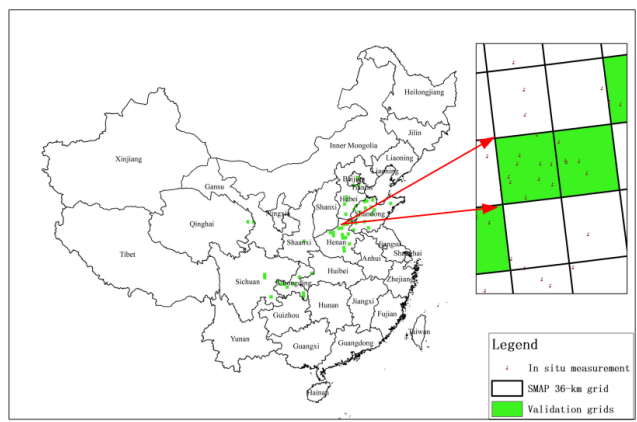
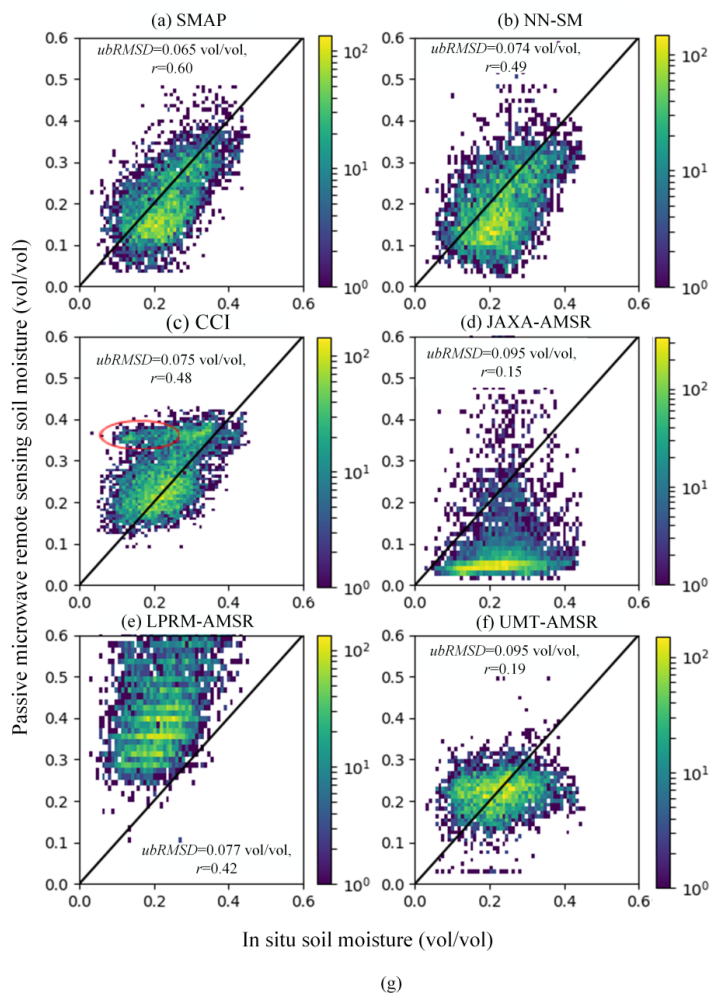
688 As manifested by Fig.A1-(a) to -(f), the selected SSM product in the current study,  
689 i.e., the NN-SM product has an unbiased RMSD of 0.074 vol/vol and a correlation  
690 coefficient of 0.49. This obviously outperforms the other three traditional AMSR-based  
691 SSM products (i.e. JAXA-AMSR, LPRM-AMSR, and UMT-AMSR products) and is  
692 only inferior to the SMAP SSM retrievals, whilst the later only covers the latest period  
693 since 2015. As far as CCI data are concerned, it has a similar performance against the  
694 selected NN-SM in general. Nevertheless, the region marked by red circle in Fig.A1-  
695 (c) indicates that CCI estimates have a considerably larger proportion of overestimated



---

696 anomalies. But overall, the primary reason that we have abandoned CCI but selected  
697 NN-SM is because the latter can provide a higher coverage fraction of valid pixels in  
698 our study region, as has been stated in Section 2.1.1.







---

700 Fig. A1 (a)-(f) Comparison of different PM SSM products (as reported in Table 1) against the in situ  
701 SSM measurements in China. (g) Locations of the 36-km EASE-GRID-projection based pixels used for  
702 this comparison campaign.

## 703 **B. Evaluation on the influence of bias adjustment for** 704 **reconstructed ‘clear-sky’ LST under cloud**

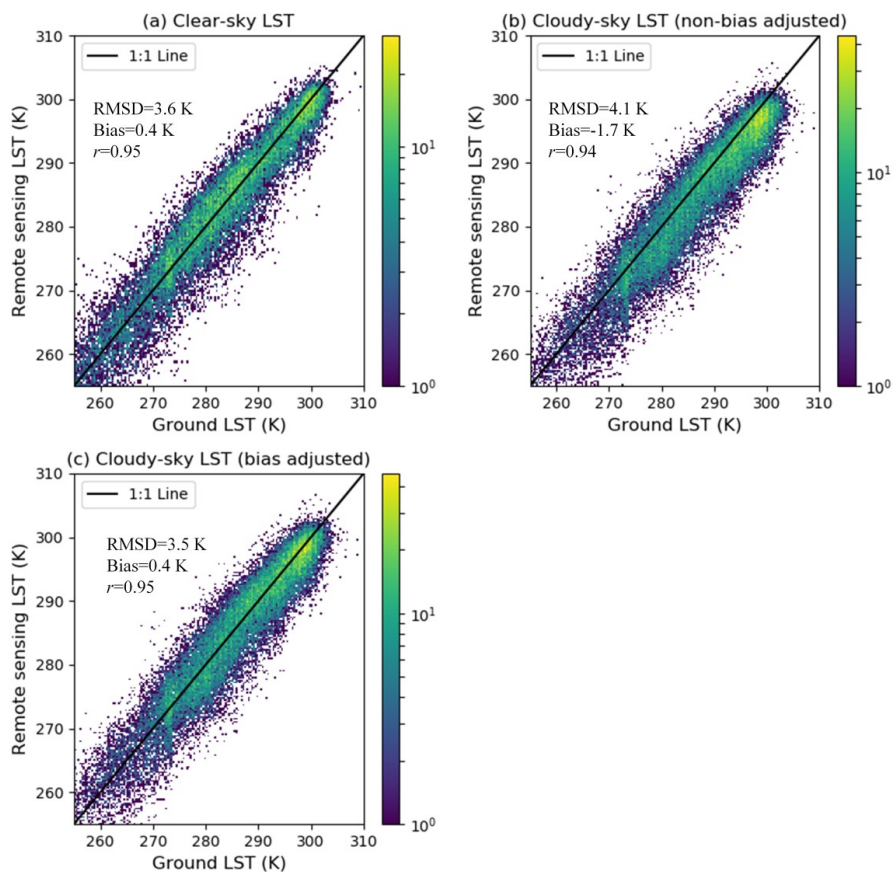
705 In Section 2.2.2, we have emphasized that the gap-filled LST for cloudy pixels  
706 reflects the theoretical surface temperature of that pixel under a hypothetical clear-sky  
707 condition. As this cloud gap-filled LST would suffer from a possible bias against the  
708 real surface temperature under cloud (Dowling et al., 2021), we made an additional  
709 experiment regarding to further improvement of this cloud gap-filled LST. The follow-  
710 up step for bias adjustment of this hypothetical clear-sky LST (but actually under  
711 cloudy conditions), as expounded in Section 4.2 of Dowling et al. (2021), was  
712 conducted herein using remote sensing and in situ LST data over China but only in  
713 2018. We illustrate the validation results for bias adjusted and non-bias adjusted LST  
714 under cloudy conditions in Fig. A2-(b) and -(c), respectively. Similar to Fig. 3,  
715 validation results for clear-sky LST of that year are also displayed (Fig. A2-(a)) for  
716 comparison. The results generally show that the follow-up step is effective in reducing  
717 the bias of the originally gap-filled ‘clear-sky LST’ under cloudy conditions (from -1.7  
718 K to 0.4 K).

719 In the subsequent step, we substituted the original non-bias adjusted LST under  
720 cloudy conditions with its bias adjusted counterpart, and used the latter as the input for  
721 SSM downscaling. The general validation results of the downscaled SSM are illustrated



---

722 in Fig. A3 (similar to that presented in Fig. 4-a and -b). Contrary to the above-analyzed  
723 Fig. A2, the bias adjusted cloudy LST with better gap-filling accuracies, however,  
724 obtained inferior performance in SSM downscaling. This final validation result, to  
725 some degree, confirms our assumption in Section 2.2.2 that the reconstructed cloudy  
726 LST but for the hypothesized clear-sky condition is the better proxy of surface moisture  
727 dynamics. But overall, as all LST estimates discussed herein are for the midnight  
728 scenario (when the energy interaction between atmosphere and land surface is relatively  
729 weak), the RMSD difference for different weather conditions in Fig.A2 is expectedly  
730 marginal. As a consequence, the difference in ubRMSD of SSM in Fig.A3 can hardly  
731 be identified as ‘very significant’. Therefore, we encourage further tests on this  
732 conclusion in specific future studies to confirm its universality, especially for situation  
733 of the ‘morning to noon’ time window.  
734



735

736

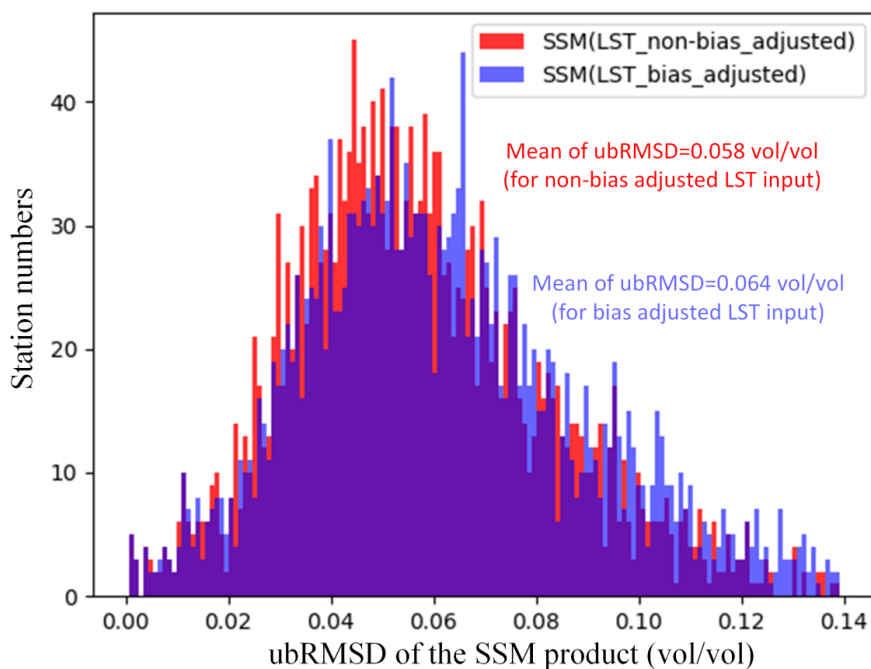
737

738

739

740

Fig. A2 Validation of the clear sky LST (a), reconstructed LST under cloud but with no passive-microwave based bias adjustment (b), as well as the reconstructed LST under cloud with passive-microwave based bias adjustment (c) respectively, based on the 0-cm ground temperature measurements at meteorological stations.



741

742 Fig. A3 The statistical distribution of ubRMSD at different stations for SSM estimates driven by two

743

respective kinds of cloudy LST inputs.

## 744 Author contributions

745 Peilin Song and Yongqiang Zhang designed the research and developed the whole

746 methodological framework; Peilin Song and Yongqiang Zhang supervised the

747 processing line of the 1-km SSM product; Jianping Guo and Bingtong provide in situ

748 soil moisture data for validation; Peilin Song wrote the original draft of the manuscript;

749 Yongqiang Zhang, Jiancheng Shi, and Tianjie Zhao revised the manuscript.

## 750 Competing interests

751 The authors declare that they have no conflict of interest.

752



---

753 **Data availability**

754 The published SSM dataset is available under the Creative Commons Attribution  
755 4.0 International License at the following link:  
756 <http://dx.doi.org/10.11888/Hydro.tpd.271762> (Song and Zhang, 2021b). This dataset  
757 covers all of China's terrestrial area at a daily revisit frequency (about 1:30 A.M. at  
758 local time) and a 1km spatial resolution from January 2003 to October 2011 and from  
759 July 2012 to December 2019.

760 **Acknowledgement**

761 The authors would like to thank the National Aeronautics and Space  
762 Administration (NASA) for providing all MODIS and DEM data sets free of charge.

763 **Financial support**

764 This study was jointly supported by the National Natural Science Foundation of  
765 China (Grant No. 42001304), the Open Fund of State Key Laboratory of Remote  
766 Sensing Science (Grant No. OFSLRSS202117), CAS Pioneer Talents Program, CAS-  
767 CSIRO International Cooperation Program, and the International Partnership Program  
768 of Chinese Academy of Sciences (Grant No. 183311KYSB20200015).  
769



---

## 770 Reference

- 771 Albergel, C., de Rosnay, P., Gruhier, C., Munoz-Sabater, J., Hasenauer, S., Isaksen, L., . . . Wagner, W.: Evaluation of  
772 remotely sensed and modelled soil moisture products using global ground-based in situ observations, *Remote Sens. Environ.*, 118,  
773 215-226, [10.1016/j.rse.2011.11.017](https://doi.org/10.1016/j.rse.2011.11.017), 2012.
- 774 Brunson, C., Fotheringham, A. S., and Charlton, M. E.: Geographically weighted regression: A method for exploring spatial  
775 nonstationarity, *Geogr. Anal.*, 28, 281-298, 1996.
- 776 Busch, F. A., Niemann, J. D., and Coleman, M.: Evaluation of an empirical orthogonal function-based method to downscale  
777 soil moisture patterns based on topographical attributes, *Hydrological Processes*, 26, 2696-2709, 2012.
- 778 Carlson, T. N., Gillies, R. R., and Perry, E. M.: A method to make use of thermal infrared temperature and NDVI  
779 measurements to infer surface soil water content and fractional vegetation cover, *Remote sensing reviews*, 9, 161-173, 1994.
- 780 Champagne, C., McNairn, H., and Berg, A. A.: Monitoring agricultural soil moisture extremes in Canada using passive  
781 microwave remote sensing, *Remote Sens. Environ.*, 115, 2434-2444, 2011.
- 782 Chauhan, N. S., Miller, S., and Ardanuy, P.: Spaceborne soil moisture estimation at high resolution: a microwave-optical/IR  
783 synergistic approach, *Int. J. Remote Sens.*, 24, 4599-4622, <http://doi.org/10.1080/0143116031000156837>, 2003.
- 784 Choi, M. and Hur, Y.: A microwave-optical/infrared disaggregation for improving spatial representation of soil moisture using  
785 AMSR-E and MODIS products, *Remote Sens. Environ.*, 124, 259-269, <http://doi.org/10.1016/j.rse.2012.05.009>, 2012.
- 786 Das, N., Entekhabi, D., Dunbar, R. S., Kim, S., Yueh, S., Colliander, A., . . . Cosh, M.: SMAP/Sentinel-1 L2 Radiometer/Radar  
787 30-Second Scene 3 km EASE-Grid Soil Moisture, Version 3 [dataset], <https://doi.org/10.5067/ASB0EQO2LYJV>, 2020.
- 788 Das, N. N., Entekhabi, D., Dunbar, R. S., Chaubell, M. J., Colliander, A., Yueh, S., . . . Thibeault, M.: The SMAP and  
789 Copernicus Sentinel 1A/B microwave active-passive high resolution surface soil moisture product, *Remote Sens. Environ.*, 233,  
790 111380, <https://doi.org/10.1016/j.rse.2019.111380>, 2019.
- 791 Dorigo, W., Himmelbauer, I., Aberer, D., Schremmer, L., Petrakovic, I., Zappa, L., . . . Sabia, R.: The International Soil  
792 Moisture Network: serving Earth system science for over a decade, *Hydrol. Earth Syst. Sci.*, 25, 5749-5804, [10.5194/hess-25-](https://doi.org/10.5194/hess-25-5749-2021)  
793 5749-2021, 2021.
- 794 Dowling, T. P. F., Song, P., Jong, M. C. D., Merbold, L., Wooster, M. J., Huang, J., and Zhang, Y.: An Improved Cloud Gap-  
795 Filling Method for Longwave Infrared Land Surface Temperatures through Introducing Passive Microwave Techniques, *Remote*  
796 *Sens.*, 13, 3522, 2021.
- 797 Du, J. Y., Kimball, J. S., and Jones, L. A.: Passive microwave remote sensing of soil moisture based on dynamic vegetation  
798 scattering properties for AMSR-E, *IEEE Trans. Geosci. Remote Sens.*, 54, 597-608, 2016.



- 
- 799** Duan, S. and Li, Z.: Spatial Downscaling of MODIS Land Surface Temperatures Using Geographically Weighted Regression:  
**800** Case Study in Northern China, IEEE Trans. Geosci. Remote Sens., 54, 6458-6469, <http://doi.org/10.1109/TGRS.2016.2585198>,  
**801** 2016.
- 802** Entekhabi, D., Reichle, R. H., Koster, R. D., and Crow, W. T.: Performance Metrics for Soil Moisture Retrievals and  
**803** Application Requirements, J. Hydrometeorol., 11, 832-840, 10.1175/2010jhm1223.1, 2010.
- 804** Entekhabi, D., Das, N., Kim, S., Jagdhuber, T., Piles, M., Yuch, S., . . . Martínez-Fernández, J.: High-Resolution Enhanced  
**805** Product based on SMAP Active-Passive Approach and Sentinel 1A Radar Data, AGU Fall Meeting Abstracts, H24C-08,  
**806** Fang, B. and Lakshmi, V.: Passive Microwave Soil Moisture Downscaling Using Vegetation and Surface Temperatures,  
**807** Vadose Zone J, 12, 1712-1717, 2013.
- 808** Fang, B., Lakshmi, V., Bindlish, R., and Jackson, T.: AMSR2 Soil Moisture Downscaling Using Temperature and Vegetation  
**809** Data, Remote Sens., 10, 2018.
- 810** Fang, B., Lakshmi, V., Bindlish, R., Jackson, T. J., Cosh, M., and Basara, J.: Passive Microwave Soil Moisture Downscaling  
**811** Using Vegetation Index and Skin Surface Temperature, 2013.
- 812** Fujii, H., Koike, T., and Imaoka, K.: Improvement of the AMSR-E Algorithm for Soil Moisture Estimation by Introducing a  
**813** Fractional Vegetation Coverage Dataset Derived from MODIS Data, Journal of the Remote Sensing Society of Japan, 29, 282-292,  
**814** 2009.
- 815** Im, J., Park, S., Rhee, J., Baik, J., and Choi, M.: Downscaling of AMSR-E soil moisture with MODIS products using machine  
**816** learning approaches, Environ Earth Sci, 75, 1-19, <http://doi.org/10.1007/s12665-016-5917-6>, 2016.
- 817** Jones, L. A., Kimball, J. S., Podest, E., McDonald, K. C., Chan, S. K., and Njoku, E. G.: A method for deriving land surface  
**818** moisture, vegetation optical depth, and open water fraction from AMSR-E, IEEE IGARSS 2009., Cape Town, South Africa, 2009,  
**819** III-916-III-919, <http://doi.org/10.1109/IGARSS.2009.5417921>.
- 820** Kim, J. and Hogue, T. S.: Improving spatial soil moisture representation through integration of AMSR-E and MODIS products,  
**821** IEEE Trans. Geosci. Remote Sens, 50, 446-460, <http://doi.org/10.1109/TGRS.2011.2161318>, 2012.
- 822** Koike, T., Nakamura, Y., Kaihotsu, I., Davva, G., Matsuura, N., Tamagawa, K., and Fujii, H.: Development of an Advanced  
**823** Microwave Scanning Radiometer (AMSR-E) algorithm of soil moisture and vegetation water content (written in Japanese), Annual  
**824** Journal of Hydraulic Engineering, 48, 217-222 2004.
- 825** Kong, D., Zhang, Y., Gu, X., and Wang, D.: A robust method for reconstructing global MODIS EVI time series on the Google  
**826** Earth Engine, Isprs J Photogramm, 155, 13-24, 2019.





- 
- 827 Malbêteau, Y., Merlin, O., Molero, B., Rüdiger, C., and Bacon, S.: DisPATCH as a tool to evaluate coarse-scale remotely  
828 sensed soil moisture using localized in situ measurements: Application to SMOS and AMSR-E data in Southeastern Australia, Int  
829 J Appl Earth Obs, 45, 221-234, <https://doi.org/10.1016/j.jag.2015.10.002>, 2016.
- 830 Meesters, A. G. C. A., De Jeu, R. A. M., and Owe, M.: Analytical derivation of the vegetation optical depth from the  
831 microwave polarization difference index, IEEE Geosci. Remote Sens. Lett., 2, 121-123, 2005.
- 832 Mendoza, P. A., Mizukami, N., Ikeda, K., Clark, M. P., Gutmann, E. D., Arnold, J. R., . . . Rajagopalan, B.: Effects of different  
833 regional climate model resolution and forcing scales on projected hydrologic changes, J. Hydrol., 541, 1003-1019,  
834 <https://doi.org/10.1016/j.jhydrol.2016.08.010>, 2016.
- 835 Meng, X. J., Mao, K. B. A., Meng, F., Shi, J. C., Zeng, J. Y., Shen, X. Y., . . . Guo, Z. H.: A fine-resolution soil moisture  
836 dataset for China in 2002-2018, Earth Syst. Sci. Data, 13, 3239-3261, 10.5194/essd-13-3239-2021, 2021.
- 837 Merlin, O., Al Bitar, A., Walker, J. P., and Kerr, Y.: An improved algorithm for disaggregating microwave-derived soil  
838 moisture based on red, near-infrared and thermal-infrared data, Remote Sens. Environ., 114, 2305-2316,  
839 <http://doi.org/10.1016/j.rse.2010.05.007>, 2010.
- 840 Merlin, O., Walker, J. P., Chehbouni, A., and Kerr, Y.: Towards deterministic downscaling of SMOS soil moisture using  
841 MODIS derived soil evaporative efficiency, Remote Sens. Environ., 112, 3935-3946, <http://doi.org/10.1016/j.rse.2008.06.012>, 2008.
- 842 Merlin, O., Chehbouni, A. G., Kerr, Y. H., Njoku, E. G., and Entekhabi, D.: A combined modeling and  
843 multi-spectral/multi-resolution remote sensing approach for disaggregation of surface soil moisture: Application to SMOS  
844 configuration, IEEE Trans. Geosci. Remote Sens., 43, 2036-2050, <http://doi.org/10.1109/TGRS.2005.853192>, 2005.
- 845 Merlin, O., Escorihuela, M. J., Mayoral, M. A., Hagolle, O., Al Bitar, A., and Kerr, Y.: Self-calibrated evaporation-based  
846 disaggregation of SMOS soil moisture: An evaluation study at 3 km and 100 m resolution in Catalunya, Spain, Remote Sens.  
847 Environ., 130, 25-38, 10.1016/j.rse.2012.11.008, 2013.
- 848 Merlin, O., Malbeteau, Y., Notfi, Y., Bacon, S., Er-Raki, S., Khabba, S., and Jarlan, L.: Performance Metrics for Soil Moisture  
849 Downscaling Methods: Application to DISPATCH Data in Central Morocco, Remote Sens., 7, 3783-3807,  
850 <http://doi.org/10.3390/rs70403783>, 2015.
- 851 Molero, B., Merlin, O., Malbêteau, Y., Al Bitar, A., Cabot, F., Stefan, V., . . . Jackson, T. J.: SMOS disaggregated soil moisture  
852 product at 1km resolution: Processor overview and first validation results, Remote Sens. Environ., 180, 361-376,  
853 <http://doi.org/10.1016/j.rse.2016.02.045>, 2016.
- 854 Montaldo, N., Albertson, J. D., Mancini, M., and Kieley, G.: Robust simulation of root zone soil moisture with assimilation of  
855 surface soil moisture data, Water Resour Res, 37, 2889-2900, 10.1029/2000WR000209, 2001.



- 
- 856** Owe, M., de Jeu, R., and Walker, J.: A methodology for surface soil moisture and vegetation optical depth retrieval using the  
**857** microwave polarization difference index, *IEEE Trans. Geosci. Remote Sens.*, 39, 1643-1654, 2001.
- 858** Peng, J., Loew, A., Zhang, S. Q., Wang, J., and Niesel, J.: Spatial downscaling of satellite soil moisture data using a vegetation  
**859** temperature condition index, *IEEE Trans. Geosci. Remote Sens.*, 54, 558-566, <http://doi.org/10.1109/TGRS.2015.2462074>, 2016.
- 860** Piles, M., Entekhabi, D., and Camps, A.: A Change Detection Algorithm for Retrieving High-Resolution Soil Moisture From  
**861** SMAP Radar and Radiometer Observations, *IEEE Trans. Geosci. Remote Sens.*, 47, 4125-4131, 10.1109/TGRS.2009.2022088,  
**862** 2009.
- 863** Sabaghy, S., Walker, J. P., Renzullo, L. J., Akbar, R., Chan, S., Chaubell, J., . . . Yueh, S.: Comprehensive analysis of  
**864** alternative downscaled soil moisture products, *Remote Sens. Environ.*, 239, 111586, <https://doi.org/10.1016/j.rse.2019.111586>,  
**865** 2020.
- 866** Sanchez-Ruiz, S., Piles, M., Sanchez, N., Martinez-Fernandez, J., Vall-llossera, M., and Camps, A.: Combining SMOS with  
**867** visible and near/shortwave/thermal infrared satellite data for high resolution soil moisture estimates, *J. Hydrol.*, 516, 273-283,  
**868** 10.1016/j.jhydrol.2013.12.047, 2014.
- 869** Scaini, A., Sanchez, N., Vicente-Serrano, S. M., and Martinez-Fernandez, J.: SMOS-derived soil moisture anomalies and  
**870** drought indices: a comparative analysis using in situ measurements, *Hydrological Processes*, 29, 373-383, 10.1002/hyp.10150,  
**871** 2015.
- 872** Song, P. and Zhang, Y.: An improved non-linear inter-calibration method on different radiometers for enhancing coverage of  
**873** daily LST estimates in low latitudes, *Remote Sens. Environ.*, 264, 112626, <https://doi.org/10.1016/j.rse.2021.112626>, 2021a.
- 874** Song, P. and Zhang, Y.: Daily all weather surface soil moisture data set with 1 km resolution in China (2003-2019), National  
**875** Tibetan Plateau Data Center [dataset], 10.11888/Hydro.tpd.271762, 2021b.
- 876** Song, P., Huang, J., and Mansaray, L. R.: An improved surface soil moisture downscaling approach over cloudy areas based  
**877** on geographically weighted regression, *Agr Forest Meteorol.*, 275, 146-158, 10.1016/j.agrformet.2019.05.022, 2019a.
- 878** Song, P., Zhang, Y., and Tian, J.: Improving Surface Soil Moisture Estimates in Humid Regions by an Enhanced Remote  
**879** Sensing Technique, *Geophys Res Lett*, 48, e2020GL091459, <https://doi.org/10.1029/2020GL091459>, 2021.
- 880** Song, P., Mansaray, L. R., Huang, J., and Huang, W.: Mapping paddy rice agriculture over China using AMSR-E time series  
**881** data, *Isprs J Photogram.*, 144, 469-482, 10.1016/j.isprs.2018.08.015, 2018.
- 882** Song, P., Huang, J., Mansaray, L. R., Wen, H., Wu, H., Liu, Z., and Wang, X.: An Improved Soil Moisture Retrieval Algorithm  
**883** Based on the Land Parameter Retrieval Model for Water-Land Mixed Pixels Using AMSR-E Data, *IEEE Trans. Geosci. Remote*  
**884** *Sens.*, 1-15, 10.1109/TGRS.2019.2915346, 2019b.



- 
- 885** Sui, D. Z.: Tobler's First Law of Geography: A Big Idea for a Small World?, *Annals of the Association of American*  
**886** *Geographers*, 94, 269-277, <https://doi.org/10.1111/j.1467-8306.2004.09402003.x>, 2004.
- 887** Wang, L. and Qu, J. J.: NMDI: A normalized multi-band drought index for monitoring soil and vegetation moisture with  
**888** satellite remote sensing, *Geophys Res Lett*, 34, L20405, 10.1029/2007GL031021, 2007.
- 889** Wei, Z., Meng, Y., Zhang, W., Peng, J., and Meng, L.: Downscaling SMAP soil moisture estimation with gradient boosting  
**890** decision tree regression over the Tibetan Plateau, *Remote Sens. Environ.*, 225, 30-44, 2019.
- 891** Wu, D., Liang, H., Cao, T., Yang, D., Zhou, W., and Wu, X.: Construction of operation monitoring system of automatic soil  
**892** moisture observation network in China, *Meteorological Science and Technology*, 42, 278-282, 2014
- 893** Yao, P., Lu, H., Shi, J., Zhao, T., Yang, K., Cosh, M. H., . . . Entekhabi, D.: A long term global daily soil moisture dataset  
**894** derived from AMSR-E and AMSR2 (2002–2019), *Scientific Data*, 8, 143, 10.1038/s41597-021-00925-8, 2021.
- 895** Zhang, Y., Kong, D., Gan, R., Chiew, F. H. S., Mervicar, T. R., Zhang, Q., and Yang, Y.: Coupled estimation of 500 m and 8-  
**896** day resolution global evapotranspiration and gross primary production in 2002-2017, *Remote Sens. Environ.*, 222, 165-182, 2019.
- 897** Zhang, Y. Q., Chiew, F. H. S., Liu, C. M., Tang, Q. H., Xia, J., Tian, J., . . . Li, C. C.: Can Remotely Sensed Actual  
**898** Evapotranspiration Facilitate Hydrological Prediction in Ungauged Regions Without Runoff Calibration?, *Water Resour Res*, 56,  
**899** 2020.
- 900** Zheng, J. Y., Lu, H. S., Crow, W. T., Zhao, T. J., Merlin, O., Rodriguez-Fernandez, N., . . . Gou, Q. Q.: Soil moisture  
**901** downscaling using multiple modes of the DISPATCH algorithm in a semi-humid/humid region, *Int J Appl Earth Obs*, 104,  
**902** 10.1016/j.jag.2021.102530, 2021.
- 903**